CONSTRUCTION MATERIAL SCIENCE

CC BY 4.0

Review article
https://doi.org/10.15828/2075-8545-2025-17-6-647-665

Strength and deformability of cement stone and Powder-activated concrete. Part II[1)]

Irina V. Erofeeva[1], Irina N. Maksimova[2]*, Dmitry A. Svetlov[3], Sergey V. Bakushev[2], Alexander I.Shein[2], Oleg V. Tarakanov[2]

[1] National Research Moscow State University of Civil Engineering, Moscow, Russia
[2] Penza State University of Architecture and Construction, Penza, Russia
[3] Soft Protector LLC, St. Petersburg, Russia

* Corresponding author: e-mail: maksimovain@mail.ru

ABSTRACT

Introduction. Reinforced concrete structures in buildings and structures are subject to various loads during operation, which cause deformation and destruction. **Materials and Methods.** It has been shown that the strength and elastic-plastic properties of modern concretes can be broadly controlled using superplasticizers, nanoadditives, fillers, and fine aggregates. This article examines the deformation and fracture processes of cement paste and powder-activated concrete. The key characteristics of concrete deformation processes are determined using stress-strain diagrams, taking into account the downward strain curve. The concrete deformation diagram on the descending branch is fixed by the ultimate deformation, corresponding to the concrete reaching its maximum strength value, and the end point of the descending branch, corresponding to the residual strength of the concrete. **Results.** Complete concrete stress-strain diagrams with an extended descending section were obtained by loading specimens at a constant, decaying strain rate, resulting in a smooth decrease in stress in the specimen along the descending section. The influence of formulation factors on the key parametric points of the σ–ε diagram was studied. The influence of the W/C ratio, modifying additive, and polycarboxylate superplasticizer on the structure-forming factors for cement stone was examined. For concrete, the influence of the W/C ratio, modifying additive, polycarboxylate superplasticizer, fine filler, rheological filler, and reactive filler was examined. The resulting diagrams were analyzed for each material structure, both with an individual structure-forming factor and for powder-activated concrete as a whole. It was found that increasing the W/C ratio from 0.267 to 0.350 resulted in more elastic behavior of the material under load, a significant (4–5 times) elongation of the descending branch of the full equilibrium stress-strain diagram of hardened cement paste, and a change in the failure mechanism of the material. The specific parameters for static destruction of the sample are reduced by 12.1 times and the static J-integral Ji is reduced by 9.1 times.. It was shown that with the addition of the carboxylate superplasticizer "Melflux 1641F," the deformation pattern of the specimen under load was closer to that of cement paste obtained using normal-thickness cement paste, however, with a shorter (10 times) descending branch, indicating more brittle behavior of the specimen. The use of finely dispersed quartz also affected the nature of the deformation of the samples: their elasticity increased from 1.3 to 1.7 times, but at the same time the magnitude of ultimate deformations decreased by 20%, that is, the samples became more elastic and less deformable. **Conclusion.** It has been established that, with optimal component contents of cement stone and powder-activated concrete, crack resistance parameters significantly increase by 1.3 to 5.8 times, especially the static J-integral Ji, which characterizes the ductile fracture energy of the material at the crack tip, increasing due to the increased adhesion of the cement stone to the active surface of the microsilica. The curves of the complete equilibrium diagrams are approximated in sections by simple linear and quadratic functions or represented by a cubic polynomial.

KEYWORDS: loading modes, hardened cement paste, powder-activated concrete, physical and mechanical properties of concrete, deformation diagrams with a descending branch, diagram approximation, differential equations

ACKNOWLEDGEMENTS: This study is supported by a 2025 grant for fundamental scientific research (R&D) by research teams at National Research Moscow State University of Civil Engineering, project №. 05-661/130.

The research was conducted using the facilities of the Main Regional Center for Collective Use of Scientific Equipment and Facilities at National Research Moscow State University of Civil Engineering with the support of the Ministry of Science and Higher Education of the Russian Federation (agreement №. 075-15-2025-549).

FOR CITATION:
Erofeeva I.V., Maksimova I.N., Svetlov D.A., Bakushev S.V., Shein A.I., Tarakanov O.V. Strength and deformability of cement stone and powder-activated concrete. Part II. *Nanotechnologies in Construction.* 2025; 17(6):647–665. https://doi.org/10.15828/2075-8545-2025-17-6-647-665. – EDN: NUJVGH.

[1)] The end. Part I was published in the journal "Nanotechnologies in Construction". 2025;17(5).

© Erofeeva I.V., Maksimova I.N., Svetlov D.A., Bakushev S.V., Shein A.I., Tarakanov O.V., 2025

CONSTRUCTION MATERIAL SCIENCE

Прочность и деформативность цементного камня и порошково-активированных бетонов. Часть II

Ирина Владимировна Ерофеева[1], Ирина Николаевна Максимова[2]*, Дмитрий Анатольевич Светлов[3], Сергей Васильевич Бакушев[2], Александр Иванович Шеин[2], Олег Вячеславович Тараканов[2]

[1] Национальный исследовательский Московский государственный строительный университет, Москва, Россия
[2] Пензенский государственный университет архитектуры и строительства, Пенза, Россия
[3] ООО «Софт Протектор», Санкт-Петербург, Россия

* Автор, ответственный за переписку: e-mail: maksimovain@mail.ru

АННОТАЦИЯ

Введение. Железобетонные конструкции в зданиях и сооружениях во время эксплуатации подвержены воздействию различных нагрузок, которые вызывают деформации и разрушения. **Материалы и методы.** Показано, что прочностные и упругопластические свойства, долговечность современных бетонов в широких пределах регулируются с помощью суперпластификаторов, нанодобавок, наполнителей и мелких заполнителей. Статья посвящена изучению процессов деформации и разрушения цементного камня и порошково-активированных бетонов. Основные характеристики процессов деформации бетонов в работе устанавливаются с помощью диаграмм «напряжение–деформация» с учетом нисходящей ветви деформации. Диаграмма деформирования бетона на нисходящей ветви фиксируется предельной деформативностью, соответствующей достижению бетоном максимального значения прочности и конечной точкой нисходящей ветви, соответствующей остаточной прочности бетона. **Результаты.** Получены полные диаграммы деформирования бетона с протяженным участком нисходящей ветви путем нагружения образцов с постоянной затухающей скоростью деформирования, при котором на нисходящем участке происходит плавное снижение напряжения в образце. Изучены зависимости влияния рецептурных факторов на основные параметрические точки диаграммы σ–ε. В качестве структурообразующих факторов для цементного камня рассматривалось влияние В/Ц-отношения, модифицирующей добавки и поликарбоксилатного суперпластификатора, а для бетонов – влияние В/Ц-отношения, модифицирующей добавки, поликарбоксилатного суперпластификатора, тонкодисперсного наполнителя, реологического и реакционного наполнителей. Выполнен анализ полученных диаграмм для каждой из структур материалов как с отдельным структурообразующим фактором, так и для порошково-активированного бетона в целом. Выявлено, что повышение В/Ц-отношения с 0,267 до 0,350 вызывает более упругое поведение материала под нагрузкой, значительное (в 4–5 раз) удлинение ниспадающей ветви полной равновесной диаграммы деформирования цементного камня и изменение механизма разрушения материала, уменьшаются в 12,1 раза удельные параметры на статическое разрушение образца и в 9,1 раза – статический джей-интеграл J_i. Показано, что при введении карбоксилатного суперпластификатора «Melflux 1641F» характер деформирования образца под нагрузкой ближе к цементному камню, полученному на цементном тесте нормальной густоты, однако с более короткой (в 10 раз) ниспадающей ветвью, что говорит о более хрупком поведении образца. Использование тонкодисперсного кварца также повлияло на характер деформирования образцов – повысилась их упругость от 1,3 до 1,7 раза, но при этом на 20% снизилась величина предельных деформаций, то есть образцы становятся более упругими и менее деформативными. **Заключение.** Установлено, что при оптимальных содержаниях компонентов цементного камня и порошково-активированного бетона существенно от 1,3 до 5,8 раза повышаются параметры трещиностойкости и особенно статический джей-интеграл J_i, характеризующий энергию вязкого разрушения материала у вершины трещины, которая возрастает вследствие повышения сцепления цементного камня с активной поверхностью микрокремнезема. Кривые полных равновесных диаграмм аппроксимированы по участкам простейшими линейными и квадратичными функциями или представляются кубическим полиномом.

КЛЮЧЕВЫЕ СЛОВА: режимы нагружения, цементный камень, порошково-активированные бетоны, физико-механические характеристики бетонов, диаграммы деформирования с нисходящей ветвью, аппроксимация диаграмм, дифференциальные уравнения

БЛАГОДАРНОСТИ: Данная работа была поддержана грантом 2025 года на проведение фундаментальных научных исследований (НИР/НИОКР) научными коллективами НИУ МГСУ, проект № 05-661/130.

Данное исследование было выполнено с использованием материально-технической базы Головного регионального центра коллективного пользования научным оборудованием и установками НИУ МГСУ при поддержке Министерства науки и высшего образования Российской Федерации (соглашение № 075-15-2025-549).

ДЛЯ ЦИТИРОВАНИЯ:
Ерофеева И.В., Максимова И.Н., Светлов Д.А., Бакушев С.В., Шеин А.И., Тараканов О.В. Прочность и деформативность цементного камня и порошково-активированных бетонов. Часть II. *Нанотехнологии в строительстве*. 2025;17(6):647–665. https://doi.org/10.15828/2075-8545-2025-17-6-647-665. – EDN: NUJVGH.

INTRODUCTION

Concrete elements and reinforced concrete structures in buildings and structures are subject to various loads during operation, which cause deformation and destruction. It has been shown that the strength and elastic-plastic properties, as well as the durability of modern concrete, can be broadly controlled using superplasticizers, nanoadditives, fillers, and fine aggregates [1–6]. The use of reactive powder concretes contributes to the production of concrete with improved physical and mechanical properties and performance characteristics [7–11].

Reactive powder concrete (RPC) is a new type of structural material with high strength, a high modulus of elasticity, and durability. These concretes do not contain coarse aggregate. Therefore, they are formed without a boundary between the transition regions between particles, which imparts higher resistance to cracking [7, 4, 12, 13]. The potential of using reactive powder concrete in steel-concrete composite beams has been proven, allowing for increased crack resistance, rigidity, and durability when replacing conventional concrete [8, 14]. A T-shaped beam constructed from reactive powder concrete of low height demonstrated high ultimate load-bearing capacity with high safety factor results (more than 2.2) [9, 10].

Russian and international researchers are working to optimize the compositions of powder concrete at the macro-, micro-, nano-, and pico-scale levels [15–18]. To date, reactive powder concrete compositions have been developed based on the fundamental principles of the physicochemistry of water-dispersed systems, primarily micrometric and, to a lesser extent, nanometric aqueous suspensions and their rheology [16, 18]. The authors have obtained micrometric suspensions of cement and rock powders and converted them into highly concentrated and aggregate-stable ones with a minimum amount of water [19–22].

Nanotechnologies for producing concrete using hydrosilicate additives are promising [23]. Progress in accelerating the hardening of cement systems using hydrosilicate crystallization nuclei has reached a high level. Currently, nanometric calcium hydrosilicates (with superfine particles) in suspension form have been synthesized both abroad and in Russia [23–25].

This article examines the deformability of hardened cement paste and reactive powder concrete. It is known that the main characteristics of material deformation and failure processes are determined using stress-strain (σ–ε) diagrams. For this purpose, various types of diagrams can be used in engineering calculations [26–29]: curvilinear, characterizing the behavior of concrete, including those with a descending branch; piecewise linear (two- and three-linear). Curvilinear diagrams characterize the relationship between stresses and strains in the form of a curvilinear line. These diagrams are used to describe the behavior of a material under plastic deformation. The effectiveness of this method when loading materials with tensile forces has been demonstrated. The characteristic points on such diagrams are the corresponding yield points (the stress at which strains increase without a noticeable increase in load) and the ultimate strength (the stress at which the material fails). Piecewise linear diagrams, which include bilinear and trilinear diagrams, are approximated by a smooth nonlinear relationship between stress and strain. This replacement of a smooth nonlinear relationship with a piecewise linear approximation significantly simplifies the solution of static objectives. These methods are used to describe the deformation behavior of microfractured, porous, and fibrous materials with elastic, viscous, and plastic properties. In particular, bilinear diagrams, which represent the relationship between stress and strain as straight sections, are also used to describe the stress-strain state of compressed concrete or tensile reinforcement. In this case, normal stresses in elastic deformation zones vary according to Hooke's law proportionally to the relative strains, while they remain constant in plastic deformation zones. The use of trilinear diagrams is effective when determining the relationship between stresses and relative strains, taking into account loads of varying duration. These types of trilinear diagrams are used to calculate the deformations of reinforced concrete elements when assessing the stress-strain state in compressed and tensile concrete using a nonlinear deformation model in the absence of cracks. This method allows for a more accurate determination of the height of the compressed zone of a section and savings in reinforcement compared to traditional calculations using a rectangular stress diagram in concrete.

The overall view and main parametric points of the σ–ε deformation diagram of concrete under compression are shown in Fig. 1.

Three regions of deformation development are distinguished in the σ–ε diagram: linear – on the ascending branch – characterizes elastic deformations (accompanied by compaction of concrete); elastic-plastic – the nonlinear section of the ascending branch – characterizes irreversible plastic deformations (accompanied by loosening of concrete); plastic stage – the descending branch of deformation – characterizes plastic deformations leading to destruction of concrete. That is, the total deformations of concrete consist of elastic (linear) and long-term (which are both reversible, obeying the principle of superposition, and irreversible, nonlinearly dependent on stresses) [30–32].

There are various interpretations of the deformation curve. V.M. Bondarenko initially proceeds from R. Olson's position that, from the point of view of the molecular-kinetic theory of the structure of solids, only a nonlinear relationship exists between stresses and strains, while a linear relationship (in the form of the well-known

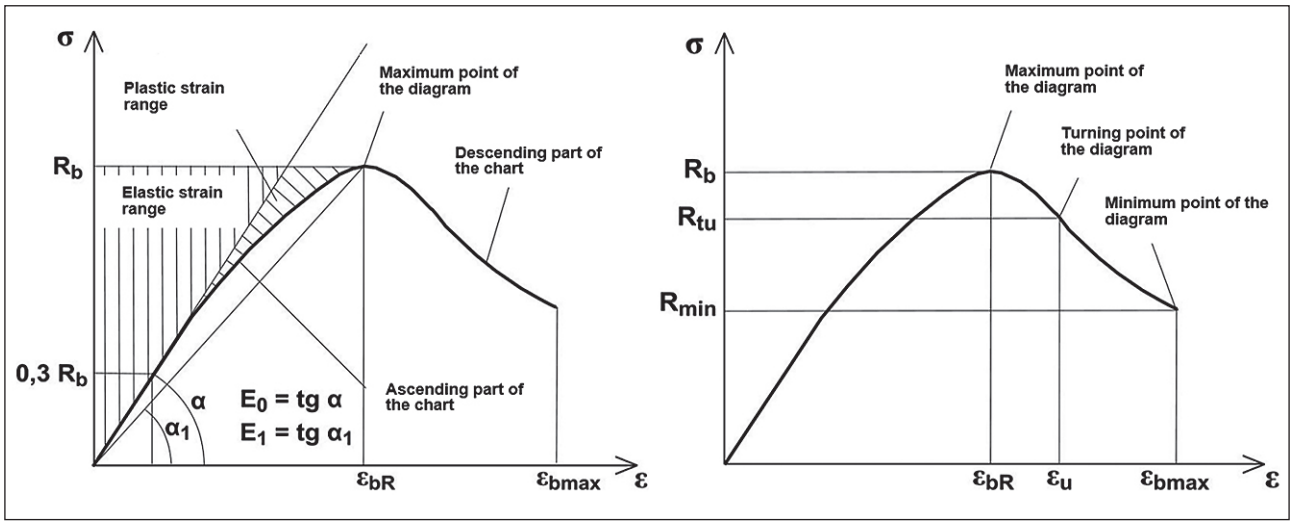

Fig. 1. Stress-strain diagram for concrete [29]

Hooke's law) is only a simplified notation of the equation of state of the material, permissible only at very low stresses [33–35]. In his works, concrete deformations are proposed to be composed of instantaneous (inelastic-nonlinear) and retarded nonlinear deformations. Therefore, he proposes his own version of the engineering calculation of reinforced concrete structures using the integral deformation modulus.

The diagrams obtained by different authors indicate that with an increase in the deformation rate, the maximum stress increases, and the corresponding ultimate deformations also increase (according to a linear law), and the time before the onset of destruction decreases according to a power law [36–41].

The heterogeneity of the concrete structure causes different relative deformations at different measurement bases. Ultimate deformations depend on the specimen size and loading conditions (the ultimate deformations of smaller specimens are greater). The diagrams of more heterogeneous materials are more distorted. To ensure reliable assessment of material quality, standards for specimen sizes and testing procedures have been established.

The modulus of elasticity (Young's modulus) is related to the straight-line region. If such a region is absent, the modulus of elasticity is tangential to the curve. Under prolonged loading, deformations can increase over time, meaning concrete exhibits plastic yield deformations. Under slow loading, concrete plastic yield partially relaxes the stress, causing stress redistribution and a change in the secondary stress field. Plastic yield develops particularly rapidly with increasing stress and ductility of the concrete and is already noticeable after a relatively short loading time. At high loading rates, the liquid phase has virtually no time to penetrate the mouths of newly forming microcracks and influence their further development. This can be observed with loading times up to failure times of less than 0.2–0.3 s.

Concrete failure occurs gradually. Initially, overstress occurs, followed by cracks in individual microvolumes, stress distribution, and the involvement of a larger volume of material in cracking, eventually leading to the formation of a continuous fracture of one type or another, depending on the shape of the specimen (structure), its dimensions, and other factors. In the final stage of loading, the microfailure process becomes unstable and takes on an avalanche-like nature.

Concrete failure under compression is caused by the development of tensile microcracks directed parallel to the applied force. An apparent increase in the volume of the specimen occurs. The process of microcrack development is determined by the structure of the concrete, as well as the type and mode of the applied load. It should be noted that the process of microcrack development in the σ_C–ε_C concrete behavior diagrams can only be detected by comparing the longitudinal and transverse deformations of the concrete specimen. Increasing crack resistance for concrete elements and reinforced concrete structures is a critical issue. This is especially important for materials and products used in the construction of high-rise buildings and structures [42], large-sized concrete beams [43], products subjected to impact loads [44], elements subjected to tensile loads [45, 46], for pile foundations [47], beam-column connections [48], prestressed beams [49], and for bridge structures [50].

Research aimed at establishing analytical expressions that best reflect the physical nonlinearity of concrete behavior under loading is relevant [51]. In this case, physical linearity is largely associated with cracks and their development. The deformative properties of concrete, taking into account the downward branch of deformation, have been examined in many studies [52, 53].

The ultimate deformability of concrete depends on various factors. The concrete deformation diagram on the descending branch is determined by the following parametric points: ε_{bR} (the ultimate deformability of concrete corresponds to the concrete reaching its maximum strength R_b), ε_{bu}, ε_{bmax} (the end point of the descending branch of the diagram corresponds to the residual strength of concrete R_{min}). The diagram evaluates various concrete states both before and after cracking. Currently, the deformation properties of powder-activated concrete, depending on the main structure-forming factors, have not been fully studied.

PURPOSE AND OBJECTIVES OF THE RESEARCH

The purpose of the study is to investigate the processes of deformation and destruction of cement stone and powder-activated concrete.

Research objectives:

1. To compile an analytical review of the works of domestic and foreign authors in the field of studying the deformability of cement stone and concrete based on stress-strain diagrams.

2. Justify the composition of cement matrices for new generation concretes for conducting research: 1) cement, ground filler, plasticizer, water (matrix of the first kind); 2) cement, ground filler, fine filler of fraction 0.1–0.5 or 0.16–0.63 mm, plasticizer, water (matrix of the second kind); 3) matrix of the first kind or matrix of the second kind, including fine filler of fraction 1.0–5.0 or 0.63–5.0 mm (matrix of the third kind).

3. To determine the influence of key structure-forming factors of cement stone and powder-activated concrete on the main parameters of crack resistance: static J-integral; specific energy costs for destruction; static stress intensity factor.

4. Obtain stress-strain diagrams for cement paste and powder-activated concrete and describe the influence of key formulation factors on the key parametric points. The type of diagrams studied should be descending-branch diagrams, which allow to examine of elastic, elastic-plastic, and plastic properties in addition to the elastic ones.

5. To study the influence of key structure-forming factors on the main physical and mechanical properties of cement stone and powder-activated concrete.

6. When studying cement stone, the influence of the water/cement ratio, modifying additive, and superplasticizer should be considered as structure-forming factors. When studying powder-activated concrete, along with the above, the influence of fine filler, rheological fillers, and reactive fillers should be considered. Analyze the resulting diagrams for materials with individual structure-forming factors, as well as for powder-activated concrete as a whole.

7. Conduct an approximation of complete equilibrium diagrams.

8. Suggest polynomial stress-strain relationships with odd integer exponents.

9. Write differential equations for typical cases of concrete deformation.

MATERIALS AND METHODS

The main binder was pure cement produced by Ulyanovsk-Cement LLC. The properties, chemical composition, and mineralogical composition of the used cement are presented in Tables 1 and 2.

The Melflux 1641F hyperplasticizer (HP) from the Melflux series (manufactured by Degussa Construction Polymers, SKW Trostberg, Germany) was used as a plasticizing additive. By structure, they are graft copolymers. They are distinguished by their electrosteric dispersion (deflocculation, agglomerate breakdown, and plasticization).

The characteristics of the hypersuperplasticizer are given in Table 1.

Stone flour was used as a rheologically active dispersed filler, and microquartz from the Lipetsk Mining and Processing Plant (LMPP) was used as the stone flour. The microquartz characteristics are presented in Table 2.

Microsilica was used as a reactive-chemical pozzolanic additive, the characteristics of which are presented in Table 3.

Sands from the Smolnensky quarry in the Ichalkovsky district of the Republic of Mordovia and the Khramtsovsky quarry in the Ivanovo region were used as fine-grained fillers and aggregate sand. The physicochemical characteristics of the fillers and the grain size distribution of the sands are presented in Tables 4–7.

Table 1. Characteristics of the hyper-superplasticizer "Melflux 1641F"

Characteristics	Melflux 1641F
External appearance, colour	Powder, color from yellowish to brown
Loss on drying, % by weight	max 2.0
Bulk density, kg/m^3	400–600
Reaction – pH 20% solution t = 20 °C	6.5–8.5
Recommended dosage in relation to the mass of the binder, %	0.05–1.0

Table 2. Microquartz characteristics

Lipetsk sand (molding)				
Sieve sizes, mm	**Residue on sieves, g**	**Partial residuals, %**	**Total residuals, %**	**Size module**
5	0	0	0	1.02
2.5	0	0	0	
1.25	0	0	0	
0.63	5	0.25	0.25	
0.315	205	10.25	10.5	
0.16	1620	81.0	91.5	
less 0.16	155	7.75	102	

Table 3. Characteristics of Lipetsk microsilica

Name of materials	SiO_2 content, %		Colour	ρ_{tr}, kg/m³	ρ_{bulk}, kg/m³	S_{spec}, kg/m³
	total	including amorphous				
Lipetsk MK-65 powder	70	60–65	Dark gray	2.3	178	6000

Table 4. Characteristics of sand from the Ichalkovsky quarry of the Republic of Mordovia

Item No.	Characteristic	Units of measurement	Indicator
1	Sand class	–	1
2	Fineness modulus	–	1.7
3	Bulk density	g/sm³	1.35
4	Content of dust and clay particles	%	2.0
5	Clay content in lumps	%	0.2
6	Filtration coefficient	m/day	3

Table 5. Characteristics of sand from the Khramtsovsky quarry in the Ivanovo region

Item No.	Name of indicators	Requirements of GOST (State Standard) 8736-2014	Actual indicators
1	Fineness modulus	2,5–3,0	2.76
2	Content of dust and clay particles, %	No more than 2.0	1.0
3	Clay content in lumps, %	No more than 0.25	Absent
4	Bulk density, kg/m³		1580
5	Content of harmful components and impurities: SO_3, % amorphous SiO_2, mmol/L	 0–1.0 0–50	 0.37 28.83
6	Specific effective activity of natural radionuclides in sand, Bq/kg	Up to 370–1st sort.	39

Table 6. Characteristics of the grain size composition of quartz sand from the Ichalkovsky quarry of the Republic of Mordovia

Residuals	Residue on sieves, %, with size of mesh, mm					
	2.5	1.25	0.63	0.315	0.16	pallet
Partial	0.28	1.11	6.44	32.16	47.34	12.67
Total	0.28	1.39	7.83	39.99	87.33	100

Table 7. Characteristics of the grain size distribution of quartz sand from the Khramtsovsky quarry in the Ivanovo region

Residuals	Residue on sieves, %, with size of mesh, mm					
	2.5	1.25	0.63	0.315	0.16	pallet
Partial	9.63	8.89	34.35	35.37	9.94	1.82
Total	9.63	18.52	52.87	88.24	98.18	100

The compositions shown in Table 8 were selected for the study.

Cement paste-based samples were prepared manually. The components were weighed before mixing. Cement and superplasticizer were weighed using an electronic scale with an accuracy of 0.01 g. When preparing the mixtures, a solution of dry superplasticizer in water was first prepared. This solution was then added to the cement. For mixtures containing superplasticizer, the amount of water was adjusted to ensure a paste of normal consistency.

Concrete mixtures were prepared using a mixer or a gravity-fed concrete mixer. Bulk concrete ingredients, namely, Portland cement, aggregates, and fillers, dosed by weight, were sequentially added to the mixer along with mixing water and a plasticizer. The mixture was thoroughly mixed until a self-compacting, homogeneous mass was obtained. The mixture was poured into standard molds and compacted on a laboratory vibrating platform. Specimens measuring 4×4×16 cm were prepared in metal molds, which were pre-lubricated with paraffin. The specimens were cured using heat and humidity treatment after curing for 24 hours in a bath with a hydraulic seal.

To obtain an equilibrium force-displacement (*F-V*) diagram for crack resistance testing of highly brittle (high-strength) specimens, a high-rigidity rig was used. Based on the force *F* and displacement *V* data, the *F-V* diagram shown in Figure 2 was constructed.

The experimental diagram was then transformed into a calculated one according to the requirements of GOST (State Standard) 29167. For this purpose, using the AutoCAD graphics editor, a stress-strain diagram was reconstructed from the data set. The algorithm for these operations is given below.

The following algorithm was adopted for determining crack resistance:

– from the beginning of the rectilinear descending section of the diagram, that is, from point *D*, where the condition *(dF/dV) ~ const* is satisfied, a segment *DK* was drawn perpendicular to the *OV* axis;
– from point *C*, a perpendicular *CH* was dropped to the *OV* axis and a line *CA*, parallel to the elastic line *OT*;
– the length of the segment *OM* was determined from the expression:

$$V_{ul}^{c} = V_e \frac{1 + 2{,}8\varphi^2}{1 + 2{,}8\varphi^2 + 6\varphi \cdot \left[\left(\frac{\lambda}{1-\lambda}\right)^2 \cdot \left(5{,}58 - 19{,}57\lambda + 36{,}82\lambda^2 - 34{,}94\lambda^3 + 12{,}77\lambda^4\right)\right]}, \quad (1)$$

where $\lambda = a_0/b$; $\varphi = b/L_0$; V_e – elastic displacements of the sample (segment AH in Fig. 2);

– from point M, a perpendicular MC_u^c was drawn to the *OV* axis until it intersected with line CC_u^c, parallel to the *OV* axis. Point *O* was connected to point C_u^c by segment OC_u^c.

The use of an equilibrium diagram allows one to determine the energy and force characteristics of the test material.

Using AutoCAD tools, we determined the areas on the equilibrium diagram that correspond to the energy costs (*W*, MJ) associated with: W_m – the processes of development and merging of microcracks before the formation of the main crack of static failure (equal to the area of *OTCA* in Fig. 2); W_e – elastic deformation before the onset of

Table 8. Basic compounds of the compositions for the preparation of samples

Components	Content of components, mass. h, for the composition					
	1	2	3	4	5	6
Ulyanovsk cement PC 500 D0	1	1	1	1	1	1
Water	0.267	0.35	0.171	0.6	0.475	0.525
GP «Melflux 1641F»	–	–	0.009	0.009	0.009	0.009
Lipetsk microsilica	–	–	–	–	0.1	–
Microquartz	–	–	–	1.1	0.75	–
Quartz sand fraction 0–0.63 mm	–	–	–	2.753	1.775	2.065
Quartz sand of fraction 0.63–2.5 mm	–	–	–	2.347	1.975	1.76

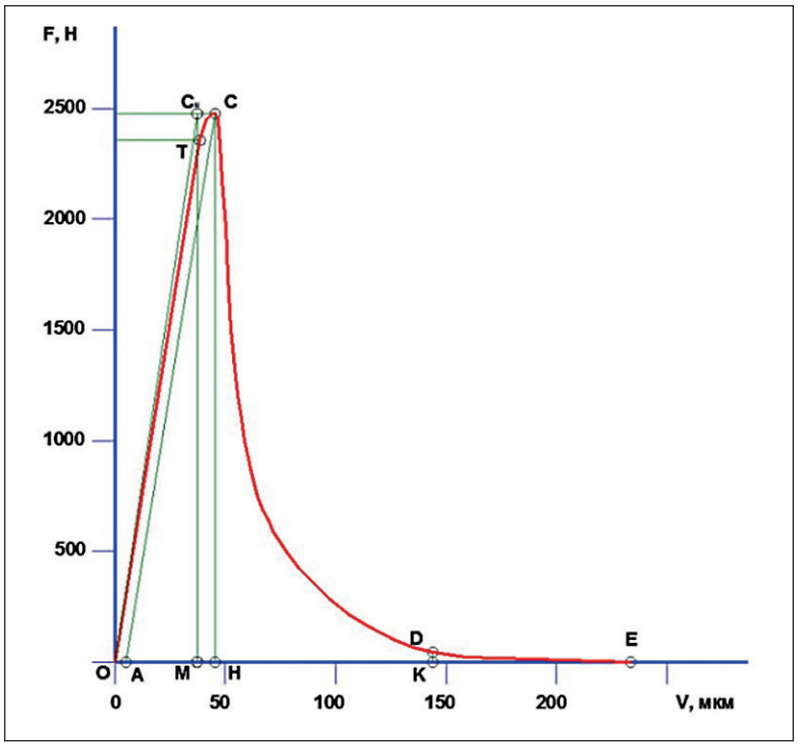

Fig. 2. Equilibrium diagram of deformation of sample № T17 [51]

movement of the main crack of static failure (equal to the area of *ACH* in Fig. 2); W_i – local static deformation in the zone of the main crack (equal to the area of *HCDK* in Fig. 2).

By calculating the area of the triangle OC^c_uM, we determined the estimated energy costs for elastic deformation of a solid sample:

$$W^c_{ui} = F_m \cdot V^c_{ui}/2, \quad (2)$$

where F_m is the maximum force achieved during the test.

The specific energy consumption values G, in MJ/m^2, were calculated using the corresponding formulas.

G_i – specific energy consumption for static destruction before the start of the main crack movement:

$$G_i = \frac{W_m + W_e}{t(b-a_0)}, \quad (3)$$

where $t = b$ are the geometric dimensions of the specimen's cross-section; a_0 is the initial crack length.

G_F is the specific effective energy consumption for static fracture:

$$G_F = \frac{W_i - W_e}{t(b-a_0)}. \quad (4)$$

G_{CE} – total specific elastic energy consumption for static deformation of samples before dividing them into parts:

$$G_{CE} = \frac{W_{CE}}{t(b-a_0)}. \quad (5)$$

The influence of technological factors on the crack resistance of concrete is assessed in two areas of the sample's operation: before the main crack starts to develop and after it starts to develop until the sample is divided into two parts.

Before the main crack starts to form, the crack resistance criteria are: W_m – energy consumption, MJ, equal to the area of the *OTCA* in Fig. 6; W_i – energy consumption, MJ, equal to the area of the *НСДК* in Fig. 2; G_i – specific energy consumption, calculated using formula (3), as well as the static J-integral, MJ/m^2, calculated using the formula

$$J_i = \frac{W_m + W_e - W_{ui}}{b(b-a_0)}. \quad (6)$$

K_i – static stress intensity factor, MPa·m$^{1/2}$:

$$K_i = \sqrt{G_i \cdot E_b}, \quad (7)$$

where the static modulus of elasticity of concrete E_b, MPa, is calculated using the formula

$$E_b = \frac{F_c}{V^c_{ui}} \frac{L^3_0}{4b^4}. \quad (8)$$

After the crack starts and until the sample is divided into two parts, the crack resistance criteria are: W_i – energy consumption, equal to the area of the *НСДК* in

Fig. 2; G_F – specific energy consumption, calculated using formula (4); K_c – critical stress intensity factor, MPa·m$^{1/2}$, calculated using the formula

$$K_C = \sqrt{G_{CE} E_b}\,. \quad (9)$$

Based on the test results, final Tables 9, 10, 11 are generated.

EXPERIMENTAL RESULTS AND THEIR ANALYSIS

This section presents the results of a study of the strength, crack resistance and deformation characteristics of cement stone and powder-activated concrete samples and an approximation of the complete equilibrium diagrams.

Equilibrium testing of the specimens was performed according to GOST (State standart) 29167–91, assessing the influence of structure-forming factors on the energy and force parameters of crack resistance. The test results are presented in Tables 12 and 13.

From the test results presented in Table 12, it follows that an increase in the water-cement ratio causes a sharp decrease primarily in the energy parameters of fracture mechanics – a decrease by a factor of 12.1 in the specific energy consumption for static fracture of the GF sample

Table 9. Determination of crack resistance characteristics of sample № T17. Initial data

Sample composition	Solidification behavior	Geometric dimensions of the sample					Sample weight, kg	Sample density, kg/m³	Humidity (weight), %
		L·10³	B·10³	H·10³	A_0·10³	L_0·10³			
T17	TBO	160	40	40	4	120	0,581	2270	3,0

Note: L – specimen length; B – width; H – height; A_0 – length of crack induced in specimen; L_0 – distance between specimen supports.

Table 10. Load values *F*, H, displacement values *V*, m, at characteristic points on the curve *"F–V"*

C		H		T		A		D		M		E	
F_c·10³	V_c·10³	F_H·10³	V_H·10³	F_T·10³	V_T·10³	F_A·10³	V_A·10³	F_D·10³	V_D·10³	F_M·10³	V_M·10³	F_E·10³	V_E·10³
2503.0	32.0	0.0	32.0	2385	18.8	0.0	11.8	22	219	0.0	18.2	0.0	278.0

Table 11. Calculated material characteristics

Energy characteristics							Crack resistance		Properties of concrete			
W_e, J	W_m, J	W_i, J	W_{ui}, J	G_i, J	G_F, J	J_i, J	K_i, MPa·м$^{1/2}$	R_{tbf}, MPa	*E*, MPa	X_{cF}, m	R_{pp}, MPa	*R*, MPa
1	2	3	4	5	6	7	8	9	10	11	12	13
0.0248	0.029 39	0.193381	0.022797	37.44375	151.5008	21.61228	0.931784	6.436214	23187.38	0.084802	6.8	10.5

Table 12. Effect of Melflux 1641F hyperplasticizer on crack resistance parameters of cement stone

Composition number	G_F		J_i		K_i	
	J/m²	Rel. unit.	J	Rel. unit.	MPa·m$^{1/2}$	Rel. unit
1	558.3	1.00	34.2	1.00	1.60	1.00
2	46.3	12.1	3.76	9.1	1.12	1.43
3	150.6	3.71 0.31	42.19	0.81 0.09	1.15	1.39 0.97

Table 13. Effect of finely dispersed quartz on crack resistance parameters of sand concrete

Composition number	W/C	G_F		J_i		K_i	
		J/m²	Rel. unit.	J	Rel. unit.	MPa·m$^{1/2}$	Rel. unit.
4	0.6	127.0	2.1	25.8	3.3	0.63	1.3
5	0.475	149.4	2.5	45.5	5.8	1.27	2.6
6	0.525	60.1	1.00	7.9	1.00	0.49	1.00

and a decrease by a factor of 9.1 in the static J-integral J_i, while the strength criterion, estimated by the value of the static stress intensity factor at normal rupture, decreased only by 1.4 times, i.e. by an amount comparable to the decrease in strength indicators (see Table 12).

As follows from the data in Table 13, the sharp decrease in the water-cement ratio caused by the use of superplasticizer led to a decrease by a factor of 3.71 in the specific energy consumption for the static destruction of the sample compared to sample № 1 and to an increase by a factor of 3.25 compared to sample № 2 with a high water content. In this case, an increase in the static J-integral J_i, which characterizes the nonlinearity of the material deformation processes at the crack tip, is observed – insignificant (by 23%) compared to the sample on the cement paste of normal density (composition № 1) and significant (by 11.22 times) – with a high water-cement ratio (composition № 2). The strength criterion, estimated by the value of the static stress intensity factor at normal rupture K_i, by analogy with the G_F criterion, has a maximum value for cement of normal consistency, i.e. both an increase and a decrease in W/C lead to a decrease in the most important parameters of crack resistance of the material.

Table 13 presents the results of comparative tests to determine the crack resistance parameters of powder-activated concrete. The results demonstrate that the use of finely dispersed quartz significantly increases the crack resistance parameters of the concrete under study—by 1.3 to 5.8 times, particularly the static J-integral *Ji*, which characterizes the ductile (plastic) fracture energy of the material at the crack tip, increasing due to the enhanced adhesion of the cement stone to the active surface of the microsilica. On the other hand, the effect of introducing finely dispersed quartz could have been even more explicit if not for the different water-cement ratio of the compositions, given that, as was established above, the influence of the water-cement factor on crack resistance parameters is not only significant, but can also be ambiguous - both a decrease and an increase in W/C relative to some rational value leads to a decrease in crack resistance of the cement stone.

The introduction of finely dispersed quartz in the form of microquartz (ground sand) and microsilica (amorphous form with a specific surface area of 50,000 sm^2/g) had a significant effect on the strength of sand concrete in bending (Table 13): the addition of microquartz (composition № 4) led to an increase in strength by 1.7 times, and the combination of microquartz and microsilica (composition № 5) – by two times.

Fig. 3, 4 show complete equilibrium diagrams of the compositions indicated in Table 8 for uniaxial compression.

The water-cement ratio also influenced the nature of the specimen's deformation under load (Fig. 3). At a lower water-cement ratio, a steeper ascending section is observed in the equilibrium deformation diagram (see Fig. 3a), which characterizes the specimen's more elastic behavior and an increased modulus of elasticity compared to hardened cement paste with a lower water-cement ratio (see Fig. 3b). However, a longer descending branch is also observed before complete failure (separation into two halves) of the beam specimen.

When using a hyperplasticizer, the deformation pattern of sample composition № 3 under load is closer to that of cement stone composition № 1 (see Fig. 3a) with a water consumption corresponding to the normal density of the cement paste, but with a shorter (10 times) descending branch, which indicates the brittle nature of the destruction of the sample (Fig. 3c).

The use of finely dispersed quartz also affected the nature of the deformation of the samples (Fig. 4) – their elasticity increased from 1.3 to 1.7 times, but at the same time the magnitude of ultimate deformations decreased by 20%, i.e., sand concrete samples become more elastic and less deformable, which is consistent with the general idea of increasing the brittleness of cement samples with an increase in their strength.

Analyzing the results of compression tests in the stress-strain axes, it can be concluded that for all the studied compositions, at the initial loading stage, the increase in stress and strain occurs according to a law close to linear, but with further deformation, the linearity is violated, and when the ultimate stress values are reached, the concrete is intensively destroyed, which is accompanied by a decrease in stress and an increase in strain.

For each composition, characteristic points with maximum stresses, beyond which specimen failure began, were identified on the resulting diagrams. The corresponding ultimate strain values (ε_{max}) were determined for these points; the transitions from the first to the second section and from the second to the third were also recorded for individual compositions.

Let us approximate the complete equilibrium deformation diagrams (Fig. 5).

In accordance with Fig. 7 and 8, the curves of the complete equilibrium diagrams should be approximated by the simplest functions – linear and quadratic – in sections.

In studies [52–54], the curves of volumetric and shear deformation of geometrically and physically nonlinear and linear continuous media were approximated by bilinear [52] and biquadratic [54] functions. This approximation made it possible to write differential equations of equilibrium in displacements for characteristic cases of deformation of a continuous geometrically and physically nonlinear and linear continuous medium: uniaxial plane deformation, axisymmetric deformation, centrally symmetric deformation, plane deformation in Cartesian and cylindrical coordinates.

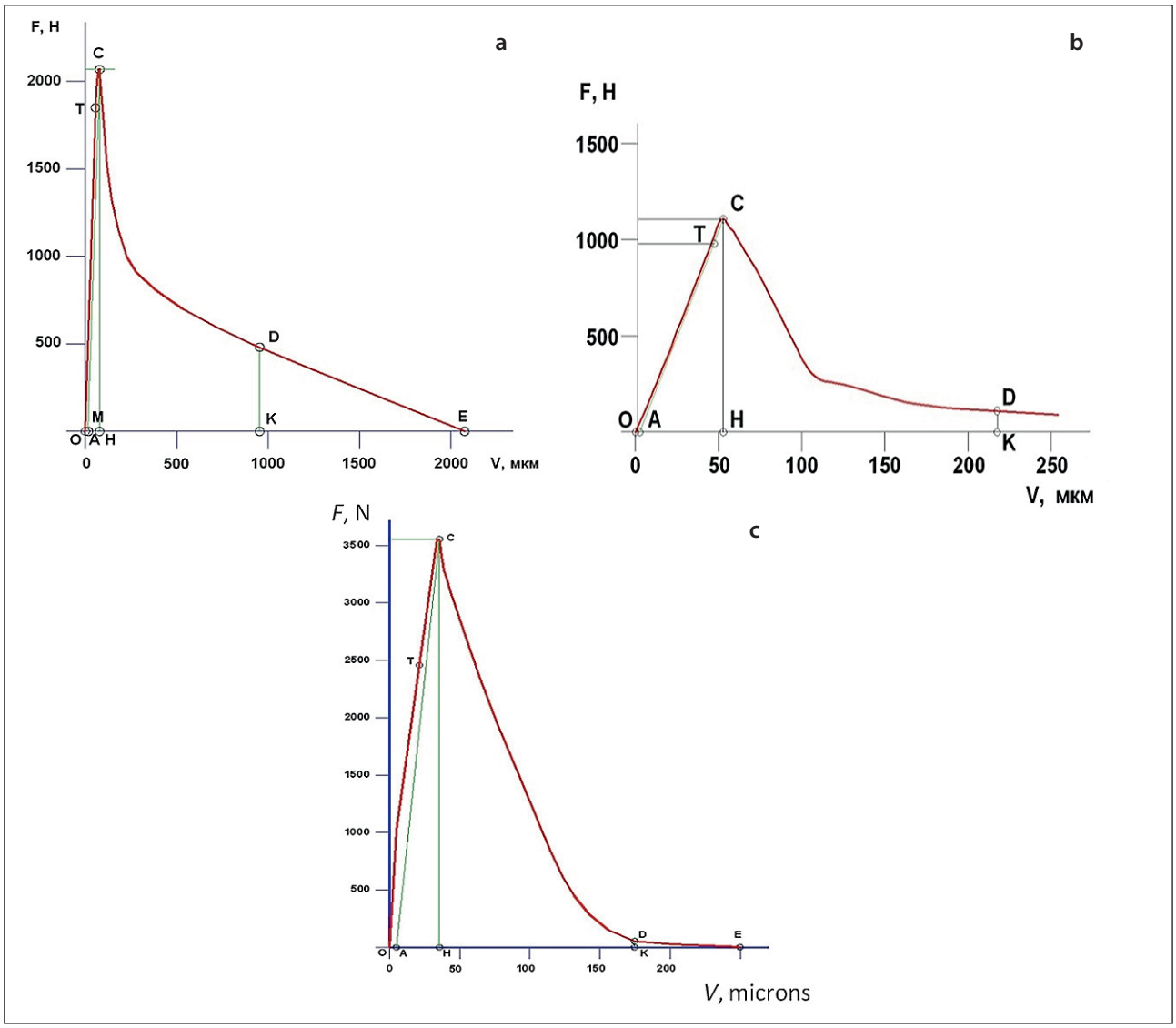

Fig. 3. Complete equilibrium diagram of deformation of cement stone of the following compositions: a – № 1; b – № 2; c – № 3

Let us highlight the main parametric points on the curves of the complete equilibrium diagrams of deformation of concrete samples (Fig. 5):

Point O – Starting point of the diagram. $\sigma_0 = 0$; $\varepsilon_0 = 0$.

Point T – The end point of the initial straight line section. σ_T; ε_T.

Point C – Maximum stress. σ_C; ε_C.

Point F – Closes the curve approximating the vertex. σ_F; ε_F.

Point D. – The point of change of curvature of the diagram. σ_D; ε_D.

Point E. – The end point of the descending branch of the diagram. σ_E; ε_E.

Let us introduce the following approximating functions:

The first section O–T is approximated by a linear function: $ax + b = y$.

The second section T–C–F is approximated by a parabola: $cx^2 + dx + e = y$.

The third section F–D is approximated by a parabola: $fx^2 + kx + l = y$.

The fourth section D–E is approximated by a linear function: $mx + n = y$.

The coefficients of the approximating functions based on the main parametric points on the curves of the complete equilibrium diagrams of deformation of concrete samples cam be determined.

The first section: $ax + b = y$

$\sigma = a\varepsilon + b$,

$0 = a \cdot 0 + b$, that is $b = 0$.

$\sigma_T = a \cdot \varepsilon_T$, that is $a = \sigma_T / \varepsilon_T$.

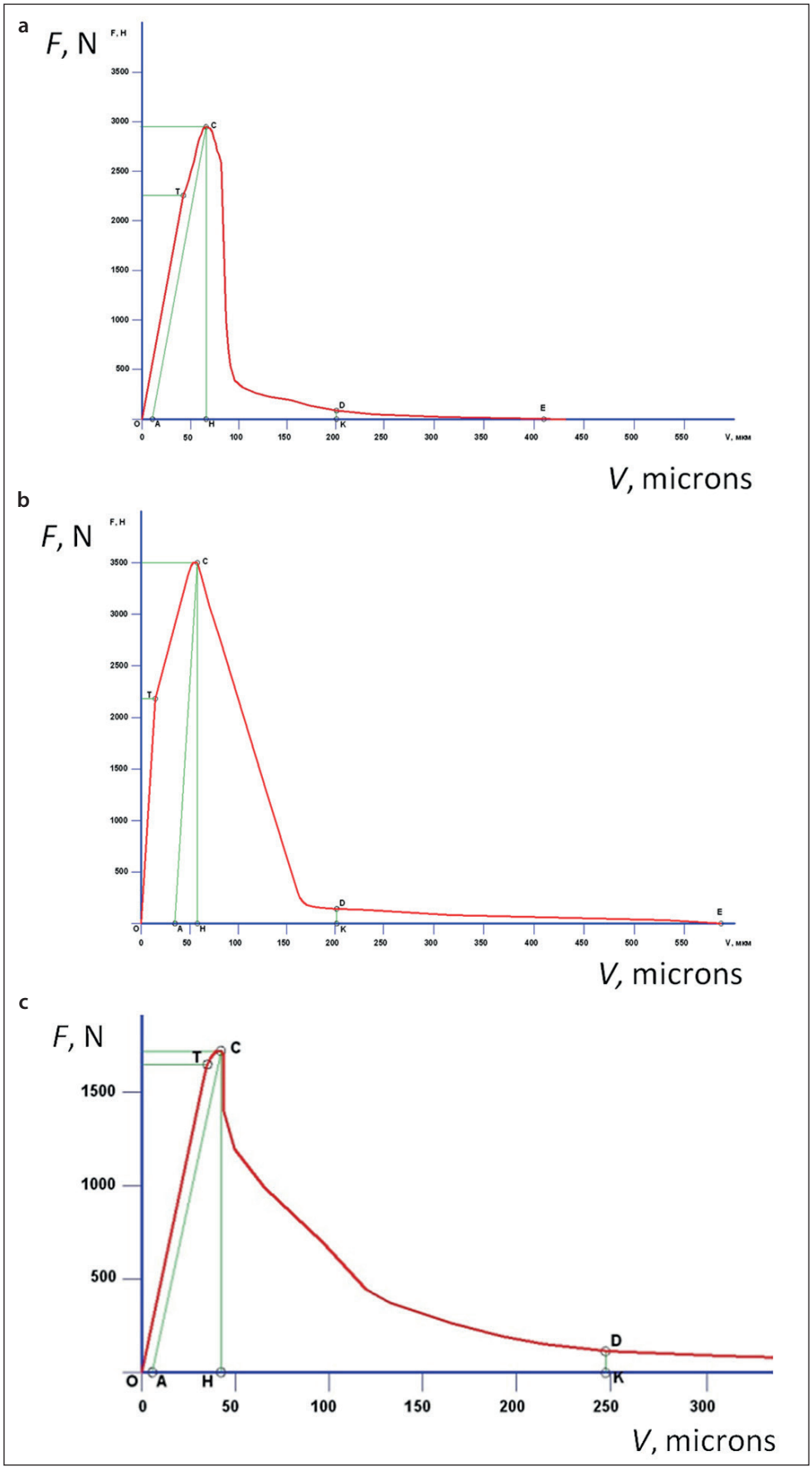

Fig. 4. Complete equilibrium diagram of deformation of sand concrete of the following compositions: a – № 4; b – № 5; c – № 6

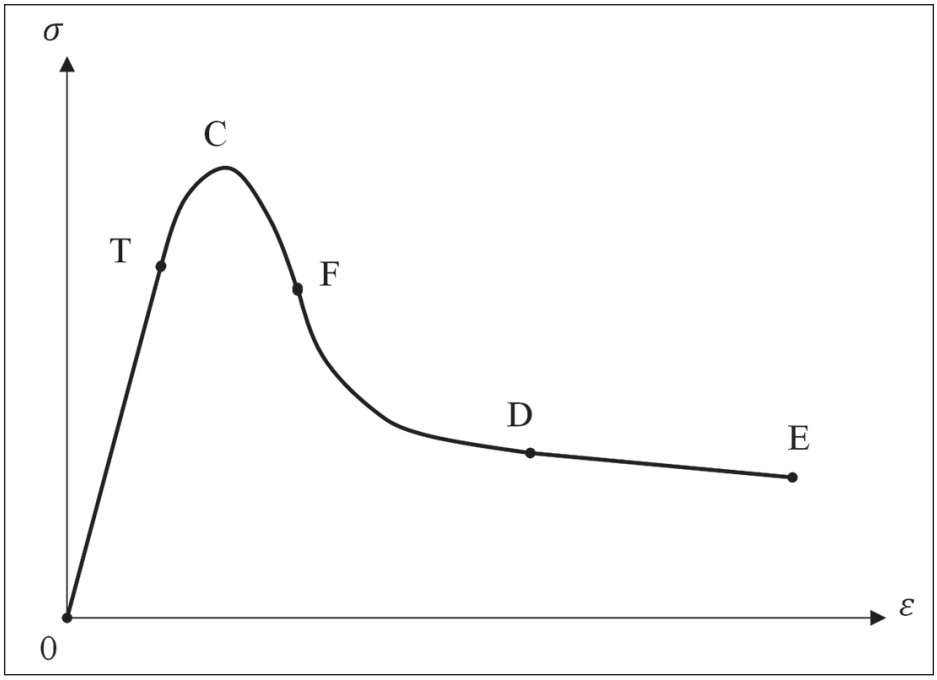

Fig. 5. Complete equilibrium deformation diagram

Summarizing:

$$\sigma = \frac{\sigma_T}{\varepsilon_T}\varepsilon. \quad (10)$$

The second section: $cx^2 + dx + e = y$
$\sigma = c\varepsilon^2 + d\varepsilon + e$,
$\sigma_T = c\varepsilon_T^2 + d\varepsilon_T + e$;
$\sigma_C = c\varepsilon_C^2 + d\varepsilon_C + e$;
$\sigma_F = c\varepsilon_F^2 + d\varepsilon_F + e$.

Solving this system of linear algebraic equations, it can be obtained:

$$\Delta = \begin{vmatrix} \varepsilon_T^2 & \varepsilon_T & 1 \\ \varepsilon_C^2 & \varepsilon_C & 1 \\ \varepsilon_F^2 & \varepsilon_F & 1 \end{vmatrix}; \Delta_1 = \begin{vmatrix} \sigma_T & \varepsilon_T & 1 \\ \sigma_C & \varepsilon_C & 1 \\ \sigma_F & \varepsilon_F & 1 \end{vmatrix};$$

$$\Delta_2 = \begin{vmatrix} \varepsilon_T^2 & \sigma_T & 1 \\ \varepsilon_C^2 & \sigma_C & 1 \\ \varepsilon_F^2 & \sigma_F & 1 \end{vmatrix}; \Delta_3 = \begin{vmatrix} \varepsilon_T^2 & \varepsilon_T & \sigma_T \\ \varepsilon_C^2 & \varepsilon_C & \sigma_C \\ \varepsilon_F^2 & \varepsilon_F & \sigma_F \end{vmatrix}.$$

Then: $c = \frac{\Delta_1}{\Delta}; d = \frac{\Delta_2}{\Delta}; e = \frac{\Delta_3}{\Delta}$.

Summarizing:

$$\sigma = \frac{\Delta_1}{\Delta}\varepsilon^2 + \frac{\Delta_2}{\Delta}\varepsilon + \frac{\Delta_3}{\Delta}. \quad (11)$$

In the second section, the branches of the parabola are directed downwards, that is, the curvature of the parabola is negative:

$$\frac{d^2\sigma}{d\varepsilon^2} = 2c = 2\frac{\begin{vmatrix} \sigma_T & \varepsilon_T & 1 \\ \sigma_C & \varepsilon_C & 1 \\ \sigma_F & \varepsilon_F & 1 \end{vmatrix}}{\begin{vmatrix} \varepsilon_T^2 & \varepsilon_T & 1 \\ \varepsilon_C^2 & \varepsilon_C & 1 \\ \varepsilon_F^2 & \varepsilon_F & 1 \end{vmatrix}} < 0.$$

This is possible if the numerator and denominator have different signs.

The third section: $fx^2 + kx + l = y$
$\sigma = f\varepsilon^2 + k\varepsilon + l$,
$\sigma_F = f\varepsilon_F^2 + k\varepsilon_F + l$;
$\sigma_D = f\varepsilon_D^2 + k\varepsilon_D + l$;
$2c\varepsilon_F + d = 2f\varepsilon_F + k$.
Solving this system of equations, it can be obtained:
$k = 2c\varepsilon_F + d - 2f\varepsilon_F$.
Then $\sigma_F = f\varepsilon_F^2 + (2c\varepsilon_F + d - 2f\varepsilon_F)\varepsilon_F + l$;
$\sigma_D = f\varepsilon_D^2 + (2c\varepsilon_F + d - 2f\varepsilon_F)\varepsilon_D + l$.
After rewriting the resulting system:
$\sigma_F = f\varepsilon_F^2 + (2c\varepsilon_F + d)\varepsilon_F - 2f\varepsilon_F^2 + l =$
$= -f\varepsilon_F^2 + l + (2c\varepsilon_F + d)\varepsilon_F$;
$\sigma_D = f\varepsilon_D^2 + (2c\varepsilon_F + d)\varepsilon_D - 2f\varepsilon_D^2 + l =$
$= -f\varepsilon_D^2 + l + (2c\varepsilon_F + d)\varepsilon_D$.
Subtracting the second from the first, we get:
$\sigma_F - \sigma_D = -f\varepsilon_F^2 + f\varepsilon_D^2 + (2c\varepsilon_F + d)(\varepsilon_F - \varepsilon_D)$.

Thus $f = \frac{(\sigma_F - \sigma_D) - (2c\varepsilon_F + d)(\varepsilon_F - \varepsilon_D)}{\varepsilon_D^2 - \varepsilon_F^2}$.

Adding the first and second, we get:
$\sigma_F + \sigma_D = -f\varepsilon_F^2 - f\varepsilon_D^2 + 2l + (2c\varepsilon_F + d)(\varepsilon_F + \varepsilon_D)$.

Thus,
$l = 1/2\ [(\sigma_F + \sigma_D) + (f\varepsilon_F^{\ 2} + f\varepsilon_D^{\ 2}) - (2c\varepsilon_F + d)(\varepsilon_F + \varepsilon_D)] = 1/2\ [(\sigma_F + \sigma_D) + f(\varepsilon_F^{\ 2} + \varepsilon_D^{\ 2}) - (2c\varepsilon_F + d)(\varepsilon_F + \varepsilon_D)]$.
Finally,

$$f = \frac{(\sigma_F - \sigma_D) - (2c\varepsilon_F + d)(\varepsilon_F - \varepsilon_D)}{\varepsilon_D^2 - \varepsilon_F^2};$$

$$k = 2c\varepsilon_F + d - 2\varepsilon_F \frac{(\sigma_F - \sigma_D) - (2c\varepsilon_F + d)(\varepsilon_F - \varepsilon_D)}{\varepsilon_D^2 - \varepsilon_F^2};$$

$$l = \frac{1}{2}\left[(\sigma_F + \sigma_D) + (\varepsilon_F^2 + \varepsilon_D^2)\frac{(\sigma_F - \sigma_D) - (2c\varepsilon_F + d)(\varepsilon_F - \varepsilon_D)}{\varepsilon_D^2 - \varepsilon_F^2} - (2c\varepsilon_F + d)(\varepsilon_F + \varepsilon_D)\right].$$

Summarizing:

$$\sigma = \frac{(\sigma_F - \sigma_D) - (2c\varepsilon_F + d)(\varepsilon_F - \varepsilon_D)}{\varepsilon_D^2 - \varepsilon_F^2}\varepsilon^2 + \left[2c\varepsilon_F + d - 2\varepsilon_F \frac{(\sigma_F - \sigma_D) - (2c\varepsilon_F + d)(\varepsilon_F - \varepsilon_D)}{\varepsilon_D^2 - \varepsilon_F^2}\right]\varepsilon + \frac{1}{2}\left[(\sigma_F + \sigma_D) + (\varepsilon_F^2 + \varepsilon_D^2)\frac{(\sigma_F - \sigma_D) - (2c\varepsilon_F + d)(\varepsilon_F - \varepsilon_D)}{\varepsilon_D^2 - \varepsilon_F^2} - (2c\varepsilon_F + d)(\varepsilon_F + \varepsilon_D)\right]. \quad (12)$$

In the third section, the curvature of the parabola is positive, that is,

$$\frac{d^2\sigma}{d\varepsilon^2} = 2f = 2\frac{(\sigma_F - \sigma_D) - (2c\varepsilon_F + d)(\varepsilon_F - \varepsilon_D)}{\varepsilon_D^2 - \varepsilon_F^2} > 0.$$

Here the denominator is positive. Then the following relation must hold:
$(\sigma_F - \sigma_D) - (2c\varepsilon_F + d)(\varepsilon_F - \varepsilon_D) > 0$.
Or $(\sigma_F - \sigma_D)/(\varepsilon_F - \varepsilon_D) > 2c\varepsilon_F + d$.
The fourth section: $mx + n = y$
$\sigma = m\varepsilon + n$.
$\sigma_D = m\varepsilon_D + n$; $\sigma_E = m\varepsilon_E + n$.
Solving this system, we obtain:
$\sigma_D - \sigma_E = m(\varepsilon_D - \varepsilon_E)$,
то есть $m = (\sigma_D - \sigma_E)/(\varepsilon_D - \varepsilon_E)$.
$\sigma_D + \sigma_E = m(\varepsilon_D + \varepsilon_E) + 2n$,
that is $n = \frac{1}{2}\left[\sigma_D + \sigma_E - \frac{\sigma_D - \sigma_E}{\varepsilon_D - \varepsilon_E}(\varepsilon_D + \varepsilon_E)\right]$.

Summarizing:

$$\sigma = \frac{\sigma_D - \sigma_E}{\varepsilon_D - \varepsilon_E}\varepsilon + \frac{1}{2}\left[\sigma_D + \sigma_E - \frac{\sigma_D - \sigma_E}{\varepsilon_D - \varepsilon_E}(\varepsilon_D + \varepsilon_E)\right]. \quad (13)$$

Thus, the complete equilibrium diagram is approximated by two straight lines and two parabolas. At point T and point D, the approximated curve may have a break; at points C and F, the curve is continuous up to second-order derivatives.

Table 14 presents the correspondences of the coefficients of the approximating polynomials for the complete equilibrium diagrams of deformation of cement stone of the compositions given in Tables 8 and 9 (composition № T17).

It is also convenient to use a simplified version of the diagram digitization.

The average σ–ε curve for concrete under short-term loading at a constant velocity is shown in Figure 6.

In this case, a descending section is detected on the diagram. When selecting and constructing approximating dependencies, we will use the concepts of ultimate compressibility $[\varepsilon^-]$ and ultimate tensile strength of concrete $[\varepsilon^+]$, i.e., concrete deformations at the moment of failure. For calculations under so-called short-term loading, we can take ultimate compressibility $[\varepsilon^-] \approx 2.0 \cdot 10^{-3}$, ultimate tensile strength under axial tension $[\varepsilon^+] \approx (1.5 \div 3) \cdot 10^{-4}$), under bending and eccentric compression $[\varepsilon^-] \approx 3.5 \cdot 10^{-3}$. Ultimate tensile strength under bending is significantly higher and edge elongations in this case can be twice as high as the previously indicated values.

When writing equilibrium equations, it is more convenient to use dependencies of the form

$$\sigma = f(\varepsilon). \quad (14)$$

In a fairly general form, such a dependence can be written as follows [56]:

$$\sigma = \sum_{i=1}^{n} A_i \cdot \varepsilon^{k_i} = A_1 \cdot \varepsilon^{k_1} + A_2 \cdot \varepsilon^{k_2} + A_3 \cdot \varepsilon^{k_3} + \cdots + A_n \cdot \varepsilon^{k_n}, \quad (15)$$

where A_i are some physical constants with the dimensions of stress; k_i are dimensionless exponents that can be any positive number (integer or fractional).

By selecting the appropriate values of A_i, k_i, and the number of terms n, any experimental diagram can be approximated with the required accuracy.

If, during deformation of a structure, stresses of different signs arise, then it is convenient to approximate the σ–ε dependence using a polynomial with integer odd exponents, for example, a cubic dependence [57]:

$$\sigma = E \cdot \varepsilon - A_3 \cdot \varepsilon^3, \quad (16)$$

ensuring the symmetry of the diagram relatively to tension-compression.

Here E is the initial modulus of elasticity of the material:

$$A_3 = \frac{4}{27}\frac{E^3}{\sigma_{nn}^2}. \quad (17)$$

Thus, when implementing the behavior of a material taking into account plastic compression deformations and taking into account tension, relation (16) can be used.

Table 14. Correspondences of the coefficients of the approximating polynomials

	First section O-T: $\sigma_0; \varepsilon_0 \sim \sigma_T; \varepsilon_T$	Second section T-C-F: $\sigma_T; \varepsilon_T \sim \sigma_F; \varepsilon_F$	Third section F-D: $\sigma_F; \varepsilon_F \sim \sigma_D; \varepsilon_D$	Fourth section D-E: $\sigma_D; \varepsilon_D \sim \sigma_E; \varepsilon_E$
Composition № 3 (Fig. 3) Type of approximating function:	Linear	Parabola. Point F is taken below point C at the break point of curve CD	Parabola	Linear. $\sigma_E = 0$
Compositions № 4, № 5, № 6. (Fig. 4) Type of approximating function:	Linear	Parabola. Point F is taken below point C at the first break point of curve CD	Parabola	Linear. $\sigma_E \neq 0$
Compositions № T17. (Fig. 2) Type of approximating function:	Linear	Parabola. Point F is taken at the level of point T.	Parabola	Linear. $\sigma_E = 0$
Compositions № T17. (Fig. 2) Type of approximating function:	Linear	Parabola. Point F is taken below point C at the first break point of curve CD	Parabola	Linear. $\sigma_E \neq 0$

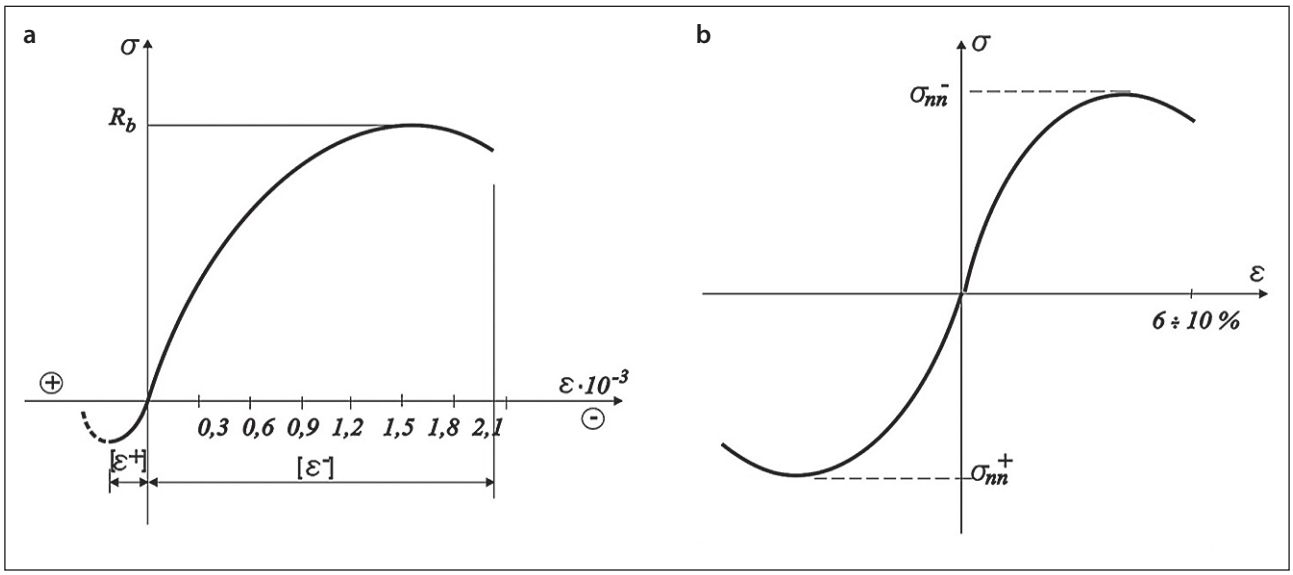

Fig. 6. Concrete deformation diagram [55]: $R_b = \sigma_{nn}$ – ultimate strength of concrete material under compression

CONCLUSION

1. A review of scientific and technical literature by domestic and foreign authors in the field of studying deformability and calculating the physical and mechanical properties of materials based on stress-strain diagrams was compiled.

2. The patterns of influence of formulation factors (W/C ratio, modifying additive, superplasticizer, fine filler, rheological and reactive fillers) on the deformability of cement stone and powder-activated concrete were established.

3. By conducting physical and mechanical tests of samples of cement stone and powder-activated concrete, stress-strain diagrams with a descending branch were obtained, which made it possible to study, along with elastic, elastic-plastic and plastic properties.

4. It was found that increasing the water-cement ratio from 0.267 to 0.350 causes more elastic behavior of the material under load, a significant (4–5 times) elongation

of the descending branch of the full equilibrium deformation diagram of cement stone, and a change in the failure mechanism of the material. An increase in the water-cement ratio causes a sharp decrease primarily in the energy parameters of fracture mechanics: a decrease by a factor of 12.1 in the specific energy consumption for static failure of the specimen GF and a decrease by a factor of 9.1 in the static J-integral J_i. Meanwhile, the strength criterion, estimated by the value of the static stress intensity factor at normal rupture, decreased only by a factor of 1.4, i.e., by an amount comparable to the decrease in strength properties (see Table 12).

5. The use of Melflux 1641F superplasticizer resulted in a significant reduction in the water-cement ratio—by a factor of 1.56 compared to the composition based on normal-thickness test and by a factor of 2.04 compared to the composition with increased water content. When using the superplasticizer, the deformation pattern of the specimen under load was closer to that of the cement paste based on normal-thickness test, but with a shorter (10 times) descending branch, indicating more brittle behavior of the specimen.

6. The use of a superplasticizer resulted in a 3.71-fold reduction in the specific energy consumption for static fracture of the specimen compared to a specimen made with normal-thickness cement paste and a 3.25-fold increase compared to a specimen with a high water content. Furthermore, an increase in the static J-integral J_i, which characterizes the nonlinearity of material deformation processes at the crack tip, was observed. The increase was insignificant (by 23%) compared to a specimen made with normal-thickness cement paste and significant (by 11.22 times) at a high water-cement ratio. The strength criterion, estimated by the value of the static stress intensity factor at normal rupture K_i, by analogy with the G_F criterion, has a maximum value for cement of normal consistency, i.e. both an increase and a decrease in W/C lead to a decrease in the most important parameters of crack resistance of the material.

7. The use of finely dispersed quartz significantly impacted the deformation behavior of the specimens—their elasticity increased by 1.3 to 1.7 times, while the ultimate deformations decreased by 20%. This means the specimens become more elastic and less susceptible to deformation. The use of finely dispersed quartz significantly increased the crack resistance parameters of the concrete studied by 1.3 to 5.8 times, particularly the static J-integral (J_i), which characterizes the ductile (plastic) fracture energy of the material at the crack tip, increasing due to the enhanced adhesion of the cement stone to the active surface of the microsilica.

8. Complete equilibrium deformation diagrams of cementitious composites were approximated by sections using linear and quadratic functions. This diagram approximation allowed us to write differential equations in displacements for typical cases of deformation of continuous media, both geometrically and physically linear and nonlinear.

REFERENCES

1. Erofeev V., Kalashnikov V., Karpushin S., (...), Tretiakov I., Matvievskiy A. Physical and mechanical properties of the cement stone based on biocidal Portland cement with active mineral additive. *Solid State Phenomena*. 2016;871:28–32. https://doi.org/10.4028/www.scientific.net/MSF.871.28

2. Maksimova I., Makridin N., Erofeev V., Barabanov D. Study of the Properties of Water-Hardened Cement Stone Depending on the Water-Cement Ratio and Age. *Lecture Notes in Civil Engineering*. 2021;150:192–203. https://doi.org/10.1007/978-3-030-72404-7_20

3. Sharafutdinov K.B., Saraykina K.A., Kashevarova G.G., Erofeev V.T. The use of copper nanomodified calcium carbonate as a bactericidal additive for concrete. *International Journal for Computational Civil and Structural Engineering*. 2022;18(2):143–155. https://doi.org/10.22337/2587-9618-2022-18-2-143-155

4. Erofeev V.T., Vatin N.I., Maximova I.N., Tarakanov O.V., Sanyagina Y.A., Erofeeva I.V., Suzdaltsev O.V. Powder-activated concrete with a granular surface texture. *International journal for computational civil and structural engineering*. 2022;18(4):49–61. https://doi.org/10.22337/2587-9618-2022-18-4-49-61

5. Sharafutdinov K., Saraikina K., Kashevarova G., Sanyagina Y., Erofeev V., Vatin N. Strength and durability of concrete with superabsorbent polymer admixture // *International Journal for Computational Civil and Structural Engineering*. 2023;19(2):120–135. https://doi.org/10.22337/2587-9618-2023-19-2-120-135

6. Tran N.P., Nguyen T.N., Ngo T.D. The role of organic polymer modifiers in cementitious systems towards durable and resilient infrastructures: a systematic review. *Construction and Building Materials*. 2022;360:129562. https://doi.org/10.1016/j.conbuildmat. 2022.129562

7. Jin L., He P., Fu Q., Chen M. Relationship of macro cracks and microstructure of RPC component. *Journal of Jiangsu University (Natural Science Edition)*. 2014;35(4):452–456 and 462. https://doi.org/10.3969/j.issn.1671-7775.2014.04.014

8. Han L.Z., Zhang J.Q., Nie J.G. Ultimate bearing capacity of steel-reactive powder concrete composite beams. *Advanced Materials Research*. 2014;900:473–482. https://doi.org/10.4028/www.scientific.net/ AMR.900.473

9. Yan Z., Ji W., An M. Design of simple-supported reactive powder concrete railway bridge with span of 32 m. *Advanced Materials Research*. 2011;163–167:904–907. https://doi.org/10.4028/www.scientific.net/ AMR.163-167.904

10. Yan Z., Ji W., An M. Experimental study and full-range analysis of Reactive Powder Concrete T-beams. *Journal of Beijing Jiaotong University*. 2009;33(1):86–90.

11. Idrees M., Akbar A., Saeed F., Saleem H., Hussian T., Vatin N.I. Improvement in durability and mechanical performance of concrete exposed to aggressive environments by using polymer. *Materials*. 2022; 15(11). https://doi.org/10.3390/ma15113751

12. Lesovik R.V., Klyuyev S.V., Klyuyev A.V., (...), Yerofeyev V.T., Durachenko A.V. Fine-grain concrete reinforced by polypropylene fiber. *Research Journal of Applied Sciences*. 2015;10(10):624–628. https://doi.org/10.3923/rjasci.2015.624.628

13. Travush V.I., Karpenko N.I., Erofeev V.T., Vatin N.I., Erofeeva I.V., Maksimova I.N., Kondrashchenko V.I., Kesarijskij A.G. Destruction of powder-activated concrete with fixation of destruction by a laser interferometer. *Magazine of Civil Engineering*. 2020;95(3):42–48. https://doi.org/10.18720/ MCE.95.4

14. Hussain H.K., Zhang L.Z., Liu G.W. An experimental study on strengthening reinforced concrete T-beams using new material poly-urethane-cement (PUC). *Construction and Building Materials*. 2013;40:104–117. https://doi.org/10.1016/j.conbuildmat.2012.09.088

15. Kalashnikov V.I. *Concretes: macro-, micro-, nano-, and pico-scale raw materials. Real nanotechnologies of concrete*. Proceedings of the conference "Days of Modern Concrete", Zaporizhzhia. 2012: 38–50.

16. Kalashnikov V.I. Evolution of the development of compositions and changes in the strength of concrete. Concrete of the present and future. Part 1. Changes in the composition and strength of concrete. *Construction materials*. 2016;1/2:96–103.

17. Kalashnikov V.I., Erofeeva I.V. High-strength concretes of the new generation. *Materials of the XII International scientific and practical conference «Science without borders»*. 2016:82–84.

18. Erofeev V., Bobryshev A., Lakhno A., (...), Sibgatullin K., Igtisamov R. Theoretical evaluation of rheological state of sand cement composite systems with polyoxyethylene additive using topological dynamics concept. *Solid State Phenomena*. 2016;871:96–103. https://doi.org/10.4028/www.scientific.net/MSF.871.96

19. Kalashnikov V.I., Erofeev V.T., Tarakanov O.V. Technical and economic efficiency of introducing architectural and decorative powder-activated carbonate sand concretes. *News of universities. Construction*. 2016;6:39–46.

20. Kalashnikov V.I., Erofeev V.T., Tarakanov O.V. Suspension-filled concrete mixes for new generation powder-activated concrete. *News of universities. Construction*. 2016;4:30–36.

21. Kalashnikov V.I., Moroz M.N., Tarakanov O.V., Kalashnikov D.V., Suzdaltsev O.V. New concepts on the mechanism of action of superplasticizers co-ground with cement or mineral rocks. *Construction materials*. 2014;9:70–75.

22. Kalashnikov V.I., Belyakova E.A., Tarakanov O.V., Moskvin R.N. Highly economical composite cement using fly ash. *Regional architecture and construction*. 2014;1:24–29.

23. Kalashnikov V.I., Erofeev V.T., Tarakanov O.V. Suspension-filled concrete mixes for new generation powder-activated concrete. *News of universities. Construction*. 2016;4(688):30–37.

24. Feng Y., Su Y., Lu N., Shah S. Meta concrete: exploring novel functionality of concrete using nanotechnology. *Engeneered Science*. October 2020. https://doi.org/10.30919/es8d816

25. Deize T, Khornuy O., Nelman M. Transition from Microdur to Nanodur technology. Application of standard cements in the production of ultra-high-performance concrete. *Concrete Plant*. 2009;3:4–10.

26. Karpenko N.I. *General models of reinforced concrete mechanics*. Moscow: Stroyizdat, 1996;407.

27. Shein A.I. Refined theory of beam systems applied to the method of mesh approximation of elements. *News of universities. Construction*. 2003;2:11–16.

28. Sobczak-Piastka J., Babych Y., Filipchuk S., Karavan V., Nalepa O. Research of deformative properties of concrete taking into account the descending branch of deformation. *IOP Conference Series: Materials Science and Engineering*. 2020;960(3):032057. https://doi.org/10.1088/1757-899X/960/3/032057

29. Rakhmanov V.A., Safonov A.A. Development of experimental methods for assessing concrete deformation diagrams under compression. *Academia. Architecture and Construction*. 2017;3:121–125.

30. Treshchev A.A., Zakharova I.A., Sudakova I.A. On options for selecting deformation diagrams for composite materials and more. *Expert: Theory and Practice*. 2022;2(17):81–90.

31. Galustov K.Z. *Nonlinear theory of concrete creep and calculation of reinforced concrete structures*. Moscow: Fizmatlit, 2006;248.

32. Maksimova I.N., Makridin N.I., Erofeev V.T., Skachkov Yu.P. *Structure and structural strength of cement composites*. Moscow: ASV, 2017;400.

33. Bondarenko V.M. *Some issues of nonlinear theory of reinforced concrete*. Kharkov: Kharkiv State University, 1968;324.

34. Bondarenko V.M., Bondarenko S.V. *Engineering methods of nonlinear theory of reinforced concrete*. Moscow: Stroyizdat, 1982;287.

35. Bondarenko V.M., Sanzharovsky R.S. On the method of calculating reinforced concrete columns. *Structural Mechanics and Calculation of Structures*. 1984;3:229.

36. Bragov A.M., Gonov M.E., Lomunov A.K., Balandin V.V. Experimental study of the dynamic properties of concrete under compressive load. Chapter 23 In: B.E.Abali and I.Giorgio (eds.), Developments and Novel Approaches in Nonlinear Solid Body Mechanics. *Advanced Structured Materials*. 2020;130:403–412. https://doi.org/10.1007/978-3-030-50460-1_23

37. Bragov A.M., Konstantinov A.Yu., Lamzin D.A., Lomunov A.K., Gonov M.E. Determination of the mechanical properties of concrete using the split Hopkinson pressure bar method. *Procedia Structural Integrity*. 2020;28:2174–2180. https://doi.org/10.1016/j.prostr.2020.11.045

38. Bragov A.M., Gonov M.E., Lamzin D.A., Lomunov A.K., Modin I.A. Response of fine-grained fiber-reinforced concretes under dynamic compression. *Materials Physics and Mechanics*. 2021;47(6):962–967. https://doi.org/10.18149/MPM.4762021_14

39. Gonov M.E., Bragov A.M., Konstantinov A.Yu., Lomunov A.K., Filippov A.R. *Features of high-speed deformation and fracture of fine-grained concrete under tensile stress*. In book: Advanced Materials Modelling for Mechanical, Medical and Biological Applications. 2021:193–211. https://doi.org/10.1007/978-3-030-81705-3_11

40. Varlamov A.A., Rimshin V.I. *Models of concrete behavior. General theory of degradation*. Moscow: INFRA-M, 2019;436.

41. Pavluk A., Gomon S., Ziatiuk Y., Gomon P., Homon S., Kulakovskyi L., Iasnii V., Yasniy O., Imbirovych N. Stiffness of solid wood beams under direct and oblique bending conditions. *Acta Facultatis Xylologiae Zvolen*. 2023;65(2):109–121.

42. Zhang L., Zhang M., Wang K., Shi J., Chen W., Yan K. Axial compressive behavior of steel-reinforced reactive powder concrete short columns. *Structures*. 2022;46:433–444. https://doi.org/10.1016/j.istruc.2022.10.073

43. Bu L., Tang D. Experimental Study and Numerical Analysis on Flexural Behavior of RC Beams Strengthened with RPC Reinforcement Mesh. *Journal of Shenyang Jianzhu University (Natural Science)*. 2022;38(4):601–609. https://doi.org/10.11717/j.issn:2095-1922.2022.04.04

44. Xu S., Wu P., Zhou F., Li Q., Zeng T., Jiang X. Experimental investigation and numerical prediction on resistance of reactive powder concrete to multiple penetration. *International Journal of Latest Technology in Engineering, Management & Applied Science*. 2016;4. https://doi.org/10.11883/bzycj-2020-0165

45. Guo M., Gao R. Relationships among the characteristic tensile strain, curing age, and strength of reactive powder concrete. *Materials*.2021;14(10):2660. https://doi.org/10.3390/ma14102660

46. Huang Y., Shi C., Ouyang X., Zhang C., Shi J., Wu Z. Research Progress on Splitting Tensile Test Methods and Mechanical Properties of Concrete. *Materials Reports*. 2021;35(1):01131–01140. https://doi.org/10.11896/cldb.20010003

47. Cheng J., Luo X., Zhuang Y., Xu L., Luo X. Experimental study on dynamic response characteristics of RPC and RC micro piles in SAJBs. *Applied Sciences*. 2019;9(13):2644. https://doi.org/10.3390/app9132644

48. Ju Y., Shen H., Wang D., Zheng W. Experimental study on crack resistance of reactive powder concrete beam-column joints. *Journal of Central South University (Science and Technology)*. 2019;50(5):1203–1209. https://doi.org/10.11817/j.issn.1672–7207.2019.05.024

49. Cui B., Wang K.-K., Zhou Q.-F., Deng K.-L., Wei L.-Y. Experiment on Static and Fatigue Performances of Assembled Concrete-steel Link in Assembled Composite Bridge Deck. *China Journal of Highway and Transport*. 2018;31(12):106–114.

50. Zhao C., Wang K., Zhou Q., Deng K., Cui B. Full-Scale Test and Simulation on Flexural Behavior of Dovetail-Shaped Reactive Powder-Concrete Wet Joint in a Composite Deck System. *Journal of Bridge Engineering*. 2018;23(8):04018051. https://doi.org/10.1061/(ASCE)BE.1943-5592.0001265

51. Erofeeva I.V. Physical and mechanical properties, biological and climatic resistance of powder-activated concrete. Abstract of dissertation for a PhD in engineering. Penza. 2018;28.

52. Bakushev S.V. Approximation of deformation diagrams by bilinear functions. *Structural mechanics and analysis of structures*. 2019;2(283):2–11.

53. Sobczak-Piastka, J., Babych, Y, Filipchuk, S, Karavan, V., Nalepa, O., 2020. Research of deformative properties of concrete taking into account the descending branch of deformation. *IOP Conference Series: Materials Science and Engineering*. 960(3), 032057.

54. Bakushev S.V. Approximation of deformation diagrams by quadratic functions. *Structural mechanics and analysis of structures*. 2020;3(290):2–14.
55. Popov N.N., Charyev M. Reinforced concrete and stone structures. Moscow: Higher School, 1996;256.
56. Bondarenko V.M., Sanzharovsky R.S. *On the method of calculating reinforced concrete columns. Structural Mechanics and Calculation of Structures*. 1984;3:74–76.
57. Lukash P.A. *Fundamentals of nonlinear structural mechanics*. Moscow: Stroyizdat. 1978;208.

ADDITIONAL INFORMATION

The authors declare that generative artificial intelligence technologies and technologies based on artificial intelligence were not used during the preparation of the article.

INFORMATION ABOUT THE AUTHORS

Irina V. Erofeeva – Cand. Sci. (Eng.), Associate Professor of the Department of Fundamentals of Architecture and Artistic Communications, National Research Moscow State University of Civil Engineering, Moscow, Russia, ira.erofeeva.90@mail.ru, https://orcid.org/0000-0003-1506-8502

Irina N. Maksimova – Cand. Sci. (Eng.), Associate Professor, Associate Professor of the Department of Quality Management, Penza State University of Architecture and Construction, Penza, Russia, maksimovain@mail.ru, https://orcid.org/0000-0001-7075-1684

Dmitry A. Svetlov – Cand. Sci. (Eng.), Director of Soft Protector LLC, St. Petersburg, Russia, svetlov@teflex.ru, https://orcid.org/0000-0002-4584-232X

Sergey V. Bakushev – Dr. Sci. (Eng.), Professor, Professor of the Department of Mechanics, Penza State University of Architecture and Construction, Penza, Russia, bakuchsv@mail.ru, https://orcid.org/0000-0001-9134-8106

Alexander I. Shein – Dr. Sci. (Eng.), Professor, Head of the Department of Mechanics, Penza State University of Architecture and Construction, Penza, Russia, shein-ai@yandex.ru, https://orcid.org/0000-0002-2797-6981

Oleg V. Tarakanov – Dr. Sci. (Eng.), Professor, Dean of the Faculty of Territory Management, Penza State University of Architecture and Construction, Penza, Russia, tarov60@mail.ru, https://orcid.org/0000-0002-1773-6095

AUTHORS' CONTRIBUTIONS

I.V. Erofeeva – scientific supervision; experimental studies; final conclusions.

I.N. Maksimova – scientific supervision; research concept; writing the original text; final conclusions.

D.A. Svetlov – research concept; writing the original text; conducting the experimental part.

S.V. Bakushev – experimental and theoretical research; final conclusions.

A.I. Shein – experimental and theoretical research; final conclusions.

O.V. Tarakanov – scientific supervision; final conclusions.

The authors declare no conflict of interest.

The article was submitted 28.08.2025; approved after reviewing 01.12.2025; accepted for publication 04.12.2025.